Available online at www.sciencedirect.com
SCIENCE DIRECT
Polymer 46 (2005) 4183–4203
polymer
www.elsevier.com/locate/polymer

# Modeling and experimental study of birefringence in injection molding of semicrystalline polymers

Kyuk Hyun Kim, A.I. Isayev*, Keehae Kwon, C. van Sweden

*Institute of Polymer Engineering, The University of Akron, Akron, OH 44325-0301, USA*

Available online 8 March 2005

This article is dedicated to Professor James E. Mark on the occasion of his 70th Birthday

**Abstract**

The prediction of birefringence developed in injection moldings is very important in order to satisfy required specification of molded products. A novel approach for the numerical simulation of the flow-induced crystallization and frozen-in birefringence in moldings of semicrystalline polymers was proposed. The approach was based on the calculation of elastic recovery that becomes frozen when the flow-induced crystallization occurred. The flow effect on the equilibrium melting temperature elevation due to the entropy reduction between the oriented and unoriented melts was incorporated to model crystallization. To find the entropy reduction and the frozen-in elastic recovery during crystallization, a non-linear viscoelastic constitutive equation was used. From the ultimate elastic recovery the crystalline orientation function was calculated. The crystalline and amorphous contributions to the overall birefringence were obtained from the crystalline orientation function and the flow birefringence, respectively. The birefringence profiles were measured and predicted in moldings of polypropylenes of different molecular weights obtained at various melt temperatures, injection speeds, holding times and mold temperatures. The resulting predictions were in fair agreement with corresponding experimental data.


*Keywords:* Viscoelastic; Birefringence; Injection molding

## 1. Introduction

The properties of polymer products are closely related to their morphology, resulting from the mechanical and thermal history experienced during the manufacturing process. Upon the imposition of deformation or strain, polymer melt flows and accumulates both the elastic and plastic strains due to the viscoelastic nature of polymer molecules. Polymer molecules are extended in the flow direction. The molecular orientation due to flow depends on the value of elastic part of the total strain. Upon the cessation of flow, the orientation reduces as the elastic strain decreases.

In amorphous polymers [1], the elastic strain or orientation freezes when the temperature goes below the glass transition temperature. In semicrystalline polymers, this condition may be reached below the crystallization temperature. The frozen-in orientation is related to the birefringence, because the molecular orientation increases the polarizability along the molecular chain.

In processing operations, such as the injection molding or extrusion, frozen-in orientations and residual stresses arise [2]. The flow-induced stresses arise from the shear and normal stresses during flow, leading to the orientation of polymer chains. If these stresses and orientations do not completely relax during the subsequent cooling period, they appear as the frozen-in birefringence and flow stresses in the products. In case of the injection molding, the extensional flow at a melt front also causes birefringence.

Residual thermal stresses arise due to the differential density or shrinkage variation and the viscoelastic behavior of the polymer during the non-uniform cooling through a glass transition or a crystallization temperature. Thermal birefringence arises due to viscoelastic behavior of polymer when it vitrifies or crystallizes. The coupling between these various stresses occurs during cooling and annealing. The degree of coupling appears to depend on the molecular conformation and is not yet completely understood. The frozen-in strains and stress patterns in injection molded

* Corresponding author. Tel.: +1 330 972 6673; fax: +1 330 258 2339.
*E-mail address:* aisayev@uakron.edu (A.I. Isayev).

0032-3861/$ - see front matter © 2005 Elsevier Ltd. All rights reserved.
doi:10.1016/j.polymer.2005.02.057

parts are more complex than those in extruded films or sheets.

In general, residual flow stresses cannot be measured directly [2–5]. However, since the flow stresses give rise to the molecular orientation, the measurement of frozen-in molecular orientation in terms of residual birefringence is an indirect indication of the residual flow stresses. That is, a distribution of flow stresses in moldings can be constructed from the birefringence measurement by the use of rheo-optical rule, relating the residual birefringence and flow stresses. This has been found to be generally true for amorphous polymers [2–7]. There are also a few attempts made to theoretically predict the residual flow stresses and correlate them with the measured frozen-in birefringence [2–5,8–12]. However, for the case of semicrystalline polymers, little information is available, related to the prediction of crystallization and its effect on the development of birefringence [13–17]. Typically predicted birefringence development does not coincide with the experimentally measured birefringence.

In the present study, the numerical simulation of the flow-induced crystallization and frozen-in birefringence in moldings of semicrystalline polymers was carried out. The approach was based on the calculation of the elastic strain that becomes frozen at the onset of crystallization. The flow effect on the equilibrium melting temperature elevation due to the entropy reduction between the oriented and unoriented melts was incorporated to model crystallization [17,18]. To find the frozen-in elastic recovery during crystallization and entropy reduction, a non-linear viscoelastic constitutive equation was used. From the elastic recovery the crystalline orientation function was calculated by using Gaylord's theoretical analysis [19]. Then crystalline and amorphous contributions to the overall birefringence were obtained from the crystalline orientation function and the flow birefringence, respectively.

## 2. Theoretical consideration

### 2.1. Governing equations

The melt delivery system and mold cavity are typically comprised of the geometric elements having either circular or rectangular cross section. Along the flow channel, geometric discontinuity occurs at the gate and junctures. The physical nature of the flow during the injection molding process in the channel allows for some simplifications of the governing transport equations for the non-isothermal flow of non-Newtonian fluids.

These may be summarized as follows:

1. The lubrication approximation is introduced. Due to small Reynolds number, inertia forces are neglected. In addition, the velocity and dynamic forces in the gapwise or radial direction are neglected along with the extensional flow arising in juncture region of mold and elongational flow at the melt front.
2. The polymer melt is assumed to be viscoelastic with the behavior obeying Leonov model [20], which incorporates temperature, time and shear rate dependence.
3. The compressibility of polymer melt, which is important during the packing stage, is taken into account by Spencer–Gilmore *PVT* equation of state [21–23]. However, without the loss of accuracy, the incompressibility of the melt is assumed during the filling stage.
4. Heat conduction is limited to the gapwise direction of a flow channel, with polymer temperature at a wall being set to that of a mold, $T_w$. Besides, heat convection is considered only along the flow direction.

The assumptions and simplifications stated above lead to Hele–Shaw type flow of the polymer melt, according to which the pressure is independent upon the gapwise (or radial) location.

The 1-D flow in a rectangular channel having the gapwise thickness of $2b$ and the width of $W$ is considered. In addition, the flow in a tube having the radius of $R$ is considered. The Cartesian coordinate system is defined such that the flow direction is designated as $x$-axis and the gapwise direction as $y$-axis. In cylindrical coordinates, the radius direction is designated as $r$-axis. The governing transport equations are:

Equation of continuity:

$$\frac{\partial \rho}{\partial t} + \frac{\partial(\rho u)}{\partial x} = 0 \tag{1}$$

Equation of motion:

$$\frac{\partial P}{\partial x} + \frac{\partial}{\partial y}\left(\eta \frac{\partial u}{\partial y}\right) = 0 \quad \text{(Cartesian coordinates)} \tag{2}$$

$$\frac{\partial P}{\partial x} + \frac{1}{r}\frac{\partial}{\partial r}\left(\eta r \frac{\partial u}{\partial r}\right) = 0 \quad \text{(cylindrical coordinates)} \tag{3}$$

Equation of energy conservation:

$$\rho C_p\left(\frac{\partial T}{\partial t} + u\frac{\partial T}{\partial x}\right) = k\frac{\partial^2 T}{\partial y^2} + \Phi + \dot{Q} \quad \text{(Cartesian coordinates)} \tag{4}$$

$$\rho C_p\left(\frac{\partial T}{\partial t} + u\frac{\partial T}{\partial x}\right) = \frac{k}{r}\frac{\partial}{\partial r}\left(r\frac{\partial T}{\partial r}\right) + \Phi + \dot{Q} \quad \text{(cylindrical coordinates)} \tag{5}$$

where $\rho$ is the density, $u$ is the velocity in the flow direction, $C_p$ is the specific heat capacity, $P$ is the pressure, $T$ is the temperature, $k$ is the thermal conductivity of the polymer, $\eta$

is the viscosity, $\Phi$ is the energy dissipation and $\dot{Q}$ is the rate of heat release due to crystallization per unit volume.

The rate of heat release due to crystallization is defined according to the crystallization kinetics as follows:

$$\dot{Q} = \rho X_\infty \Delta H_c \frac{d\theta}{dt} \tag{6}$$

where $X_\infty$ is the ultimate degree of crystallinity, $\Delta H_c$ is the heat of fusion per unit mass for the pure crystal and $\theta$ is the relative degree of crystallinity.

For a viscoelastic flow, the energy dissipation function is [24]:

$$\Phi = 2s\eta_0 \,\mathrm{tr}(\bar{\bar{E}}^2) + \sum_{k=1}^{N} \frac{\eta_k}{4\theta_k^2}\left[\frac{I_C^k(II_C^k - I_C^k)}{3} + \mathrm{tr}(C_{ij,k}^2) - 3\right] \tag{7}$$

where $\bar{\bar{E}}$ is the deformation-rate tensor, $s$ is the dimensionless rheological parameter lying between zero and unity, $\eta_0$ is the zero-shear-rate viscosity, $\eta_k$ is the shear viscosity of the $k$th mode, $I_C^k$ and $II_C^k$ are the first and the second invariant of the elastic strain tensor, $C_{ij,k}$, and $\theta_k$ is the relaxation time.

Leonov multi-mode non-linear constitutive equation was used to describe the rheological behavior of polymer melts [20]:

$$C_{ij,k}^{\nabla} + \frac{1}{2\theta_k}[C_{ij,k}^2 + \frac{1}{3}(II_C^k - I_C^k)C_{ij,k} - \bar{\bar{I}}] = 0 \tag{8}$$

where $\bar{\bar{I}}$ is the identity tensor and $C_{ij,k}^{\nabla}$ is the Jaumann derivative.

The deformation-rate tensor and the zero-shear-rate viscosity may be expressed as

$$\bar{\bar{E}} = \frac{1}{2}\{\nabla\bar{u} + (\nabla\bar{u})^{\mathrm{T}}\} \tag{9}$$

$$\eta_0(T) = \frac{\sum_{k=1}^{N}\eta_k(T)}{1-s} \tag{10}$$

The viscosity and the relaxation time are assumed to have an Arrhenius-type temperature dependence:

$$\eta_k(T) = A_k \exp\left(\frac{T_b}{T}\right) \tag{11}$$

$$\theta_k(T) = B_k \exp\left(\frac{T_b}{T}\right) \tag{12}$$

where $T_b$ is the temperature sensitivity related to the activation energy and $A_k$, $B_k$ are constants.

These values may increase dramatically as the polymer crystallizes. However, the crystallinity effect on the viscosity and relaxation time was not considered in this study.

In case of simple shear, the elastic strain tensor has the following form:

$$C_{ij,k} = \begin{bmatrix} C_{11,k} & C_{12,k} & 0 \\ C_{12,k} & C_{22,k} & 0 \\ 0 & 0 & 1 \end{bmatrix} \tag{13}$$

For 1-D incompressible case in the filling stage, the conservation of mass and momentum may be expressed as [2]:

$$\frac{\partial}{\partial x}\left(S\frac{\partial P}{\partial x}\right) = 0 \tag{14}$$

where fluidity $S$ is defined as:

$$S = \int_0^b \frac{y^2}{\eta}\mathrm{d}y \quad \text{(Cartesian coordinates)} \tag{15}$$

$$S = \frac{1}{2}\int_0^R \frac{r^3}{\eta}\mathrm{d}r \quad \text{(cylindrical coordinates)} \tag{16}$$

The average velocity, $\bar{u}$, can be expressed as

$$\bar{u} = \frac{1}{b}\int_0^b u\,\mathrm{d}y \quad \text{(Cartesian coordinates)} \tag{17}$$

$$\bar{u} = \frac{2}{R^2}\int_0^R ru\,\mathrm{d}r \quad \text{(cylindrical coordinates)} \tag{18}$$

According to the $N$-mode Leonov model, the stress tensor $\tau_{ij}$ is then given by:

$$\tau_{ij}(y,t) = 2\mu\theta_1(T)s\dot{\gamma}\begin{bmatrix} 0 & 1 & 0 \\ 1 & 0 & 0 \\ 0 & 0 & 0 \end{bmatrix} + 2\sum_{k=1}^{N}\mu_k(T)\begin{bmatrix} C_{11,k} & C_{12,k} & 0 \\ C_{12,k} & C_{22,k} & 0 \\ 0 & 0 & 1 \end{bmatrix} \tag{19}$$

where $\dot{\gamma} = -\partial u/\partial y$ is the shear rate, $\mu_k = \eta_k/2\theta_k$ is the modulus of $k$th mode and $\mu = \eta_0/2\theta_1$.

The governing equation for $C_{ij,k}$ in Eq. (8) can be expressed in the component form as:

$$\frac{\mathrm{D}C_{11,k}}{\mathrm{D}t} - 2C_{12,k}\frac{\partial u}{\partial y} + \frac{1}{2\theta_k}(C_{11,k}^2 + C_{12,k}^2 - 1) = 0 \tag{20}$$

$$\frac{\mathrm{D}C_{12,k}}{\mathrm{D}t} - C_{22,k}\frac{\partial u}{\partial y} + \frac{1}{2\theta_k}(C_{11,k} + C_{22.k})C_{12,k} = 0 \tag{21}$$

$$C_{11,k}C_{22,k} - C_{12,k}^2 = 1 \tag{22}$$

with D/D$t$ being the material derivative operator.

Introducing the pressure gradient, $\Lambda$, the shear stress, $\tau_{12}$, can be expressed by:

$$\tau_{12} = \Lambda y = \eta\dot{\gamma} \quad \text{(Cartesian coordinates)} \tag{23}$$

$$\tau_{12} = \frac{\Lambda r}{2} = \eta\dot{\gamma} \quad \text{(cylindrical coordinates)} \tag{24}$$

On the other hand, by integrating Eq. (17) (Cartesian) or Eq. (18) (cylindrical) by part, and eliminating $\dot{\gamma}$ using Eq. (23) (Cartesian) or Eq. (24) (cylindrical), it follows:

$$\bar{u} = \frac{\Lambda}{b}\int_0^b \frac{y^2}{\eta}\mathrm{d}y = \frac{\Lambda}{b}S \quad \text{(Cartesian coordinates)} \tag{25}$$

$$\bar{u} = \frac{\Lambda}{R^2}\int_0^R \frac{r^3}{2\eta}\mathrm{d}r = \frac{\Lambda S}{R^2} \quad \text{(cylindrical coordinates)} \tag{26}$$

Accordingly, from Eqs. (17), (19), (23) and (25) for Cartesian coordinates, or from Eqs. (18), (19), (24) and (26) for cylindrical coordinates, $\Lambda$ can be expressed as

$$\Lambda(t) = \frac{\left(2\mu s b\bar{u} - 2\sum_{k=1}^{N}\mu_k \int_0^b \frac{yC_{12,k}}{\theta_1}\mathrm{d}y\right)}{\int_0^b \frac{y^2}{\theta_1}\mathrm{d}y} \quad \text{(Cartesian coordinates)} \tag{27}$$

$$\Lambda(t) = \frac{\left(4\mu s R^2\bar{u} - 4\sum_{k=1}^{N}\mu_k \int_0^R \frac{r^2C_{12,k}}{\theta_1}\mathrm{d}r\right)}{\int_0^R \frac{r^3}{\theta_1}\mathrm{d}r} \quad \text{(cylindrical coordinates)} \tag{28}$$

The elastic strain tensor components at a steady state flow, $C_{ij,k}^{\mathrm{st}}$, can be expressed by:

$$C_{11,k}^{\mathrm{st}} = \frac{\sqrt{2}X_k}{\sqrt{1+X_k}} \tag{29}$$

$$C_{12,k}^{\mathrm{st}} = \frac{2\dot{\gamma}X_k}{1+X_k} \tag{30}$$

$$C_{22,k}^{\mathrm{st}} = \frac{\sqrt{2}}{\sqrt{1+X_k}} \tag{31}$$

where $X_k = 1 + \sqrt{1+4(\dot{\gamma}\theta_k)^2}$.

The shear viscosity can be expressed as

$$\eta = \eta_0 s + \sum_{k=1}^{N}\frac{2\eta_k}{1+\sqrt{1+4(\dot{\gamma}\theta_k)^2}} \tag{32}$$

In order to consider the compressibility during the packing stage, Spencer–Gilmore thermodynamic equation of state [21–23] can be used as:

$$(P+\bar{P})\left(\frac{1}{\rho}-\frac{1}{\bar{\rho}}\right) = \hat{R}T \tag{33}$$

The specific volume for semicrystalline polymers can be calculated from Eq. (33) as:

$$V(T,P) = \frac{1}{\rho(T,P)} = \frac{1}{\bar{\rho}} + \frac{\bar{R}}{P+\bar{P}}T + \frac{1}{\bar{\rho}_t} \tag{34}$$

where a typical *PVT* curve is comprised of two linear regions of rubbery and glassy state separated at the glass transition temperature including the density compensation term, $\bar{\rho}_t$, to handle the sharp density change in the vicinity of crystallization temperature, $T_t$ as proposed in [25]. Material constants, $\bar{\rho}$, $\bar{R}$, $\bar{P}$, are different for the rubbery and glassy states. They can be determined from two separate fits to experimental data.

Eq. (34) can be expressed in two separate regions as follows:

if $T \geq T_t$

$$\frac{1}{\bar{\rho}_t} = b_7\exp(b_8\bar{T} - b_9P), \quad \bar{\rho} = \bar{\rho}_1;\ \bar{R} = \bar{R}_1;\ \bar{P} = \bar{P}_1 \tag{35}$$

if $T < T_t$

$$\frac{1}{\bar{\rho}_t} = 0, \quad \bar{\rho} = \bar{\rho}_s;\ \bar{R} = \bar{R}_s;\ \bar{P} = \bar{P}_s \tag{36}$$

with

$$T_t = b_5 + b_6P \quad \text{and} \quad \bar{T} = T - b_5 \tag{37}$$

where $b_5$, $b_6$, $b_7$, $b_8$, $b_9$, and, $\bar{\rho}_1$, $\bar{R}_1$, $\bar{P}_1$ and $\bar{\rho}_s$, $\bar{R}_s$, $\bar{P}_s$ are fitted material parameters at the above and below the phase transition temperature for semicrystalline polymers.

For a semicrystalline polymer like PP, a typical *PVT* curve consists of two linear regions of the rubbery and glassy state with a transition zone in between. The specific volume at the transition region as a function of crystallinity as well as temperature and pressure is calculated by:

$$V(T,P,X_c) = X_cV_s(T,P) + (1-X_c)V_l(T,P) \tag{38}$$

where $V_l$ and $V_s$ are the specific volume above and below the transition temperature and $X_c$ is the absolute degree of crystallinity.

Since the specific volume depends on the pressure and temperature one can write:

$$\frac{\partial\rho}{\partial t} = \left(\frac{\partial\rho}{\partial P}\right)_T\frac{\partial P}{\partial t} + \left(\frac{\partial\rho}{\partial T}\right)_P\frac{\partial T}{\partial t} \tag{39}$$

where

$$\left(\frac{\partial\rho}{\partial P}\right)_T = \frac{\rho}{P+\hat{P}}\left(1-\rho\hat{\rho}\right) \tag{40}$$

$$\left(\frac{\partial\rho}{\partial T}\right)_P = -\frac{\rho}{T}\left(1-\rho\hat{\rho}\right) \tag{41}$$

Assuming no slip condition at the mold wall and the geometric symmetry of the flow channel, appropriate boundary conditions for the velocity and temperature could be specified as follows:

$$u|_{y=b,\ y=R} = 0, \quad \frac{\partial u}{\partial y}|_{y=0} = 0 \tag{42}$$

$$T|_{y=b,\ y=R} = T_w, \quad \frac{\partial T}{\partial y}|_{y=0} = 0 \tag{43}$$

Since pressure $P$ is assumed to be independent of $y$-position, the integration of Eq. (2) over $y$ (Cartesian) or Eq. (3) over $r$ (cylindrical), with the incorporation of Eq. (42), gives:

$$\dot{\gamma} = -\frac{\partial u}{\partial y} = \frac{\Lambda y}{\eta} \quad \text{(Cartesian coordinates)} \tag{44}$$

$$\dot{\gamma} = -\frac{\partial u}{\partial r} = \frac{\Lambda r}{2\eta} \quad \text{(cylindrical coordinates)} \tag{45}$$

where $\Lambda$ represents the pressure gradient along the flow direction. That is,

$$\Lambda = -\frac{\partial P}{\partial x} \tag{46}$$

Further, by integrating Eq. (44) (Cartesian) or Eq. (45) (cylindrical) and making use of Eq. (42), one can get:

$$u = \Lambda \int_y^b \left(\frac{y}{\eta}\right) \mathrm{d}y \quad \text{(Cartesian coordinates)} \tag{47}$$

$$u = \Lambda \int_r^R \left(\frac{r}{2\eta}\right) \mathrm{d}r \quad \text{(cylindrical coordinates)} \tag{48}$$

One may treat the density $\rho(x,y,t)$ in Eq. (1) as a representative quantity $\bar{\rho}(x,t)$ that is independent of the gapwise position, and neglect the convective term, $u(\partial\rho/\partial x)$, on the left-hand side of the equation. Integrating Eq. (2) over $y$ from 0 to $b$, and making use of Eqs. (46) and (47) will result in [2]:

$$\frac{\partial(\ln \bar{\rho})}{\partial t} = \frac{1}{b}\frac{\partial}{\partial x}\left(S\frac{\partial P}{\partial x}\right) \tag{49}$$

where

$$\bar{\rho} = \frac{1}{b}\int_0^b \rho(x,y,t)\mathrm{d}y \tag{50}$$

Eq. (49) is the governing equation for the 1-D flow combining both the continuity and momentum equations. It should be noted that all variables in the equation are independent of the gapwise direction. Therefore, Eq. (49) is utilized for updating the pressure profile $P(x,t)$ as a function of $x$-coordinate and time.

The complete injection molding process can be divided into three typical stages, namely the filling, packing and cooling. The filling and packing stages are simulated by numerically solving both the unified governing equation of flow, Eq. (49), and equation of energy conservation, Eq. (4), while the simulation of the cooling stage is similar to that of the packing stage by assuming no flow in this stage.

### 2.2. Onset of flow-induced crystallization

For simplicity, the instantaneous nucleation is assumed which makes the use of a detailed nucleation model unnecessary. Such an assumption has been proposed for the case of the flow-induced crystallization where the crystallization driving forces are large [26,27].

In order to determine the highly oriented skin layer developed during the molding cycle, it is important to know the onset of flow-induced crystallization. For an oriented polymer melt, the reduction in entropy, due to the orientation of polymer molecules under flow, causes the elevation of equilibrium melting point, $T_m^o$.

According to Flory [28] this elevated melting temperature, $T_m$, can be calculated as:

$$\frac{1}{T_m} = \frac{1}{T_m^o} - \frac{\Delta S_{el}}{\Delta H_f} \tag{51}$$

where $\Delta S_{el}$ is the change of entropy, and $\Delta H_f$ is the change of enthalpy of crystallization. The value of $\Delta H_f$ is the difference between the heat released by crystallization, $\Delta H_f^m$, and the created interfacial energy, $\Delta H_f^A$:

$$\Delta H_f = \Delta H_f^m - \Delta H_f^A = f_{cr}\Delta H_f^m \tag{52}$$

The crystallization factor, $f_{cr}$, is introduced as the crystallization enthalpy change divided by the heat of crystallization. Evidently, the crystallization factor is affected by the created interfacial energy. Therefore, this value is very important in the flow-induced crystallization. As a result, the temperature elevation by the oriented polymer melt can be expressed through the combination of the entropy reduction and heat of crystallization [17,18]:

$$\frac{1}{T_m} = \frac{1}{T_m^o} - \frac{\Delta S_{el}}{f_{cr}\Delta H_f^m} \tag{53}$$

The entropy reduction in Eq. (53) is related to the first invariant of the $k$th mode of the elastic strain tensor, $I_C^k$ [17,18]:

$$\Delta S_{el} = \sum_k \frac{\mu_k}{T\rho}[I_C^k - 3] \tag{54}$$

where $I_C^k = C_{11,k} + C_{22,k} + C_{33,k}$.

This invariant can be obtained by solving the governing equations for $C_{ij,k}$ during the filling, packing and cooling stage.

It should be noted that Flory equation, Eq. (51), was derived based on the equilibrium statistical physics. On the other hand, Eq. (54) for the calculation of entropy reduction is based upon the strain invariant derived from the constitutive equation obtained from the irreversible thermodynamics. Therefore, in applying Eq. (51), we assume that the non-equilibrium process at any flow condition is treated as an equilibrium process.

### 2.3. Crystallization rate constant

A number of papers concerning various effects observed during the crystallization of polymers in the oriented or deformed states have been published. A thermodynamic description, first presented by Flory [28], was extended by Kobayashi and Nagasawa [29] and Gaylord [30]. These theories predict an increase of the equilibrium melting temperature mainly due to the entropy reduction of the deformed macromolecular system. Attempts have been also made to take into account the effect of external stress on the

rate of crystallization [31–34]. On a qualitative basis this effect was confirmed by many experiments [35–37].

For an oriented melt, the flow-induced crystallization takes place as soon as $T_m$ reaches the local temperature. The elevated melting temperature $T_m$ increases the degree of supercooling, hence speeds up the crystallization process. It means that the elevation of melting temperature has the same effect as the supercooling does in crystallization kinetics. This supercooling effect of flow on the crystallization rate can be incorporated into the non-isothermal Nakamura equation [38,39] through rate constant determined from the modified Hoffman–Lauritzen equation [40] by replacing $T_m^o$ with $T_m$. Ishizuka et al. [35] estimated the orientation dependence of nucleation and growth rate by replacing the isotropic melting temperature in the non-isothermal crystallization equation with the elevated melting temperature due to the orientation. Dunning [41] expressed the rate of nucleation as a function of the degree of supercooling by replacing the isotropic melting temperature in the non-isothermal crystallization equation with the elevated temperature due to the extension and experimentally confirmed this effect. Guo and Nahr [42] and Isayev et al. [17] applied the modified Hoffman–Lauritzen equation and Nakamura equation to simulate the flow-induced crystallization in the injection molding process.

The modified Nakamura equation is:

$$\frac{D\theta}{Dt} = nK_s(T,\dot{\gamma})(1-\theta)[-\ln(1-\theta)]^{(n-1)/n} \tag{55}$$

where $n$ is Avrami exponent and $K_s(T,\dot{\gamma})$ is the modified crystallization rate constant affected by the shear rate:

$$K_s(T,\dot{\gamma}) = (\ln 2)^{1/n}\left(\frac{1}{t_{1/2}}\right)_0 \exp\left(\frac{-U^*/R}{T-T_\infty}\right) \times \exp\left(-\frac{K_k}{T(T_m(T,\dot{\gamma})-T)f}\right) \tag{56}$$

with

$$f = \frac{2T}{T+T_m(T,\dot{\gamma})}, \quad T_\infty = T_g - 30 \tag{57}$$

where $T_m(T,\dot{\gamma})$ is from Eq. (53), $f$ is a correction factor for the reduction in the latent heat of fusion as the temperature is decreased, $R$ is the universal gas constant, $U^*$ is the activation energy for segmental jump of polymer molecules and may be assigned a universal value of 6284 J/mol, $(1/t_{1/2})_0$ is a temperature independent pre-exponential factor that includes all terms influencing the crystallization process and $K_k$ is the nucleation exponent. From Eq. (53) it is evident that $T_m$ increases the degree of supercooling and therefore the crystallization rate.

### 2.4. Birefringence development during crystallization

The birefringence is the measure of the difference in the polarizability of molecular chains in two perpendicular directions, which is related to the chain orientation.

In case of semicrystalline polymer, the overall birefringence, $\Delta n$, is the sum of the contribution of the crystalline region, $\Delta n_c$, and that of the amorphous region, $\Delta n_a$, and the form birefringence, $\Delta n_f$:

$$\Delta n = \Delta n_c + \Delta n_a + \Delta n_f = X_c f_c \Delta n_c^o + (1-X_c) f_a \Delta n_a^o + \Delta n_f \tag{58}$$

where $\Delta n_c^o$ and $\Delta n_a^o$ are the intrinsic crystalline and amorphous birefringence, respectively, $f_c$ and $f_a$ are the crystalline and amorphous orientation functions, respectively. In the present study, the contribution of $\Delta n_f$ is neglected.

During molding the orientation at every point of the molded article can be characterized by the following symmetric tensor of refractive index [43]:

$$n_{ij} = \begin{pmatrix} n_{11} & n_{12} & n_{13} \\ n_{12} & n_{22} & n_{23} \\ n_{13} & n_{23} & n_{33} \end{pmatrix} \tag{59}$$

For 1-D flow this tensor can be simplified to:

$$n_{ij} = \begin{pmatrix} n_{11} & n_{12} & 0 \\ n_{12} & n_{22} & 0 \\ 0 & 0 & n_{33} \end{pmatrix} \tag{60}$$

The simplest way to define the state of frozen-in orientation in the molded part is to measure the three mutually independent components of birefringence:

$$\Delta n = \sqrt{(n_{11}-n_{22})^2 + 4n_{12}^2}, \quad n_{11}-n_{33}, \quad \text{and} \quad n_{22}-n_{33} \tag{61}$$

corresponding to the three mutually perpendicular planes $xy$, $xz$ and $yz$, respectively (with 1 or $x$, 2 or $y$, 3 or $z$ corresponding to the flow, gapwise, and width directions of the cavity).

When the polymer is in the amorphous state, the magnitude of the birefringence due to flow, $\Delta n_{flow}$, assumed to be equal to $\Delta n_a$, is proportional to that of the imposed principal stress. This flow birefringence can be calculated using the rheo-optical rule [2,6]:

$$\Delta n_a = \Delta n_{flow} = C\sqrt{N_1^2 + 4\tau_{12}^2} = (1-X_c) f_a \Delta n_a^o \tag{62}$$

where $C$ is the constant stress-optical coefficient, $N_1$ is the first normal stress difference. In semicrystalline polymers the overall birefringence depends on the flow history and the viscoelastic properties of the polymer melts until the flow-induced crystallization takes place and the relaxation of molecular orientation ceases. At the onset of crystallization, the molecular chains may lose their fluidity, and the stress as well as the elastic strain may freeze. The molecular orientation, which results from the frozen-in elastic strain,

becomes part of the crystalline contribution to the overall orientation. The molecular orientation in an amorphous region also freezes with freezing of elastic strain when the relaxation process becomes complete. This flow birefringence is the contribution of amorphous region to the overall birefringence. Then, the overall birefringence in Eq. (58) becomes:

$$\Delta n = \Delta n_{\mathrm{c}} + \Delta n_{\mathrm{flow}} = X_{\mathrm{c}} f_{\mathrm{c}} \Delta n_{\mathrm{c}}^{\mathrm{o}} + C\sqrt{N_1^2 + 4\tau_{12}^2} \tag{63}$$

The magnitude of the molecular orientation is the result of the frozen-in elastic strain, which is assumed to be equal to the elastic recovery. It is postulated here that this elastic recovery can be used as a measure of orientation to calculate the birefringence contribution of the crystalline region of semi-crystalline polymers.

The total strain, $\gamma_{\mathrm{total}}$, can be divided into two components, the elastic, $\gamma_{\mathrm{e}}$, and inelastic (plastic) strain, $\gamma_{\mathrm{p}}$:

$$\gamma_{\mathrm{total}} = \gamma_{\mathrm{e}} + \gamma_{\mathrm{p}} \tag{64}$$

The elastic strain is associated with the orientation of polymer molecules, whereas the plastic strain is related to the intermolecular chain slippage, which is related to the flow. Flow-induced crystallization leads to an abrupt increase of the melt viscosity, and hence a loss of fluidity. Therefore, one can assume that the recoverable elastic strain freezes at the moment of crystallization. The magnitude of this elastic strain can be used to calculate the crystalline orientation function. At the start of flow the elastic strain component dominates, whereas the plastic strain component dominates at the later stage. When the crystallization occurs, the stress-optical rule is no longer applicable, and the crystalline birefringence cannot be calculated.

Thus in this research, the frozen-in elastic recovery was used to calculate the birefringence contribution from the crystalline region. The frozen-in elastic strain was determined using the non-linear viscoelastic constitutive equation [20].

The elastic recovery is the part of total shear strain which is recovered after unloading the stress. The transient, $\gamma_t(x,y,t)$, and the ultimate, $\gamma_\infty(x,y)$, elastic recovery can be expressed as [44]:

$$\gamma_t(x,y,t) = \int_0^t \dot{\gamma}(x,y,\xi)\mathrm{d}\xi \tag{65}$$

$$\gamma_\infty(x,y) = \int_0^\infty \dot{\gamma}(x,y,\xi)\mathrm{d}\xi \tag{66}$$

where $\dot{\gamma}$ is the shear rate variation with time during recovery. The elastic recovery can be obtained by letting the value of shear stress, $\tau_{12}$, in Eq. (19) be zero, and one obtains [44]:

$$\dot{\gamma}(x,y,t) = \frac{-1}{s\mu\theta_1(T)} \sum_{k=1}^{N} \mu_k C_{12,k}(x,y,t) \tag{67}$$

The shear rate expressed in Eq. (67) is substituted into the governing equations for $C_{ij,k}$ in Eqs. (20)–(21):

$$\frac{\mathrm{D}C_{11,k}}{\mathrm{D}t} + \frac{2}{s\mu\theta_1} C_{12,k} \sum_{i=1}^{N} \mu_i C_{12,i} + \frac{1}{2\theta_k}(C_{11,k}^2 + C_{12,k}^2 - 1) = 0 \tag{68}$$

$$\frac{\mathrm{D}C_{12,k}}{\mathrm{D}t} + \frac{1}{s\mu\theta_1} C_{22,k} \sum_{i=1}^{N} \mu_i C_{12,i} + \frac{1}{2\theta_k}(C_{11,k} + C_{22.k})C_{12,k} = 0 \tag{69}$$

Eqs. (68), (69) and (22) can be solved for $C_{ij,k}$ by starting from the fully-developed flow using the steady-state initial conditions in Eqs. (29)–(31) [44]. Then the shear rate can be obtained from Eq. (67). Finally, the elastic recovery is obtained by integrating the shear rate with respect to time in Eqs. (65) and (66).

The obtained elastic recovery, $\gamma_\infty$, was used to calculate the principal extension ratios, $\lambda$. For the simple shear, these values are as follows [45]:

$$\lambda_1 = \lambda; \quad \lambda_2 = 1; \quad \lambda_3 = 1/\lambda \tag{70}$$

$$\lambda = \frac{\gamma_\infty + \sqrt{\gamma_\infty^2 + 4}}{2} \tag{71}$$

where $\lambda_1$, $\lambda_2$ and $\lambda_3$ are the principal stretch ratio to $x$, $y$ and $z$ direction, respectively.

According to Gaylord's theoretical analysis of the flow-induced crystallization in Gaussian networks, the crystalline orientation function is related to $\lambda$ as [1,30]:

$$f_{\mathrm{c}} = \frac{1}{2}\left(\frac{3\lambda^3}{2+\lambda^3} - 1\right) \tag{72}$$

Certainly, this approach for the calculation of $f_{\mathrm{c}}$ is oversimplified since it is applicable to the uniaxial extension. In the injection molding, the crystalline orientation function is more complicated. However, for the simplicity we use Gaylord approach in the calculation of $f_{\mathrm{c}}$ in this study. This function determined at the onset of the crystallization was used to predict the crystalline contribution to the overall birefringence in Eq. (63).

## 3. Experimental

### 3.1. Materials and sample preparation

The materials studied are various commercial i-PPs with different molecular weights, namely Pro-fax PP-6523, PP-6723 and PP-6823 that are simply the homopolymers with a general purpose stabilization package, supplied by Basell.

The general material characteristics, including melt flow index (MFI), polydispersity index (PI), and weight-averaged molecular weight ($M_w$) are given in Table 1. Model parameters related to the crystallization kinetics, the non-linear viscoelastic constitutive equation, and the thermal properties are given in Table 2.

A Van Dorn injection molding machine model Van Dorn-50F series with a standard tensile bar as shown in Fig. 1 was used for the experiments. The pressure was monitored by three piezoelectric pressure transducers Kistler 6153B at positions close to sprue (position P1), gate (position P2) and the end of the cavity (position P3). When the pressure was applied, the pressure transducer produced charge, which was amplified and monitored by a charge monitor, Kistler 5058B. The output voltage from the amplifier to the data acquisition card is between 0 and 10 V. The experiments were done at various processing variables, such as, inlet melt temperature ($T_0$), injection speed ($V_{inj}$), holding pressure ($P_h$), holding time ($t_h$) and mold temperature ($T_w$). For each material, the injection molding experiments were performed at 8 processing conditions as shown in Table 3 [46]. The gapwise birefringence distributions of $\Delta n$ in moldings were measured by Van Sweden [46].

### 3.2. Quiescent crystallization

To characterize crystallization kinetics for various materials used in this study, sufficiently dried pellet was used. Approximately 10 mg of material was prepared from the pellet and used for both isothermal and non-isothermal crystallization characterization. The isothermal characterization was carried out using the sample in a nitrogen atmosphere by means of Perkin–Elmer differential scanning calorimeter (DSC-7). The sample was first heated from room temperature to a specific temperature (210 °C) sufficiently above the melting temperature and annealed for 10 min in the DSC furnace in order to erase any thermal and mechanical history. The melt was cooled at a rate of 60 °C/min until the specified crystallization temperature was reached. The half time, $t_{1/2}$, when half of the final crystallinity is achieved was measured. In case of non-isothermal crystallization characterization, a sample was first heated from room temperature to 210 °C and annealed for 10 min in the DSC furnace as in the isothermal case. The melt was then cooled at a specific rate (2.5, 5, 10, 20 and 40 °C/min) down to a room temperature, and the relative degree of crystallinity as a function of time and temperature was obtained using a non-isothermal thermogram. Then by applying the master curve approach to crystallization kinetics developed in [47], the experimental rate constants as a function of temperature were obtained. These rate constant data were fitted to Hoffman–Lauritzen equation to determine crystallization kinetics model parameters, $(1/t_{1/2})_0$ and $K_k$ which are listed in Table 2.

Table 1
Materials specification

| Materials | PP-6523 | PP-6723 | PP-6823 |
|---|---|---|---|
| MFI (dg/min) | 4.1 | 0.92 | 0.51 |
| PI | 4.3 | 3.9 | 3.9 |
| $M_w$ | 351,000 | 557,000 | 670,000 |

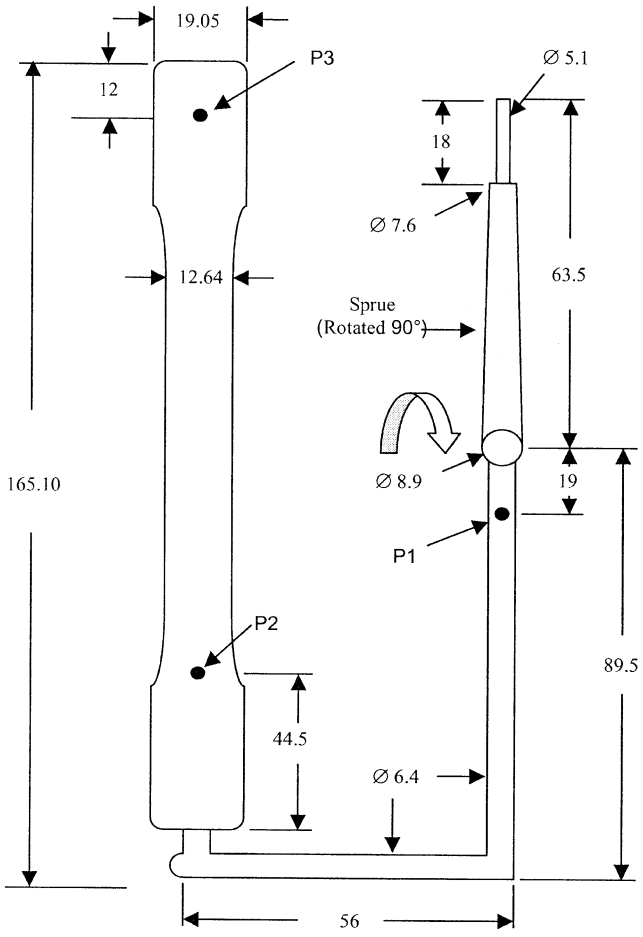


Fig. 1. Mold used in experiments. All dimensions are given in mm. P1, P2 and P3 indicate the positions of pressure transducers.

Experimental data and fitted curves for PP-6523, -6723, and -6823 are illustrated in Fig. 2 [15].

### 3.3. Rheological characterization

In order to calculate the rate constant for the flow-induced crystallization based on the thermodynamical crystallization model and density variation, occurring during the injection molding cycle, various material parameters are required. These include physical, thermal and rheological properties, and the parameter of the crystallization model listed in Table 2. The rheological (flow curve) measurements were performed on a Rheometrics mechanical spectrometer (RMS-800) in the cone-and-plate mode within the low shear rates ranging from $10^{-2}$ to 2.0 $s^{-1}$ and on an Instron capillary rheometer (Model 3211) within the high shear rates from 10 to $10^3$ $s^{-1}$. The

Table 2
Model parameters related to crystallization kinetics, constitutive equation, and thermal properties of iPPs

| Material constants | PP-6523 | PP-6723 | PP-6823 | Reference |
|---|---|---|---|---|
| *Crystallization kinetics* | | | | |
| $(1/t_{1/2})_o \times 10^{-8}$ ($s^{-1}$) | 5.459 | 3.858 | 1.528 | [15] |
| $K_k \times 10^{-5}$ ($K^2$) | 3.99 | 3.93 | 3.81 | [15] |
| $n$ | 3 | 3 | 3 | |
| $\Delta H_c$ (J/g) | 110.56 | 96.10 | 91.02 | [46] |
| $X_\infty$ | 0.5290 | 0.4598 | 0.4355 | [46] |
| $f_{cr}$ | 0.11 | 0.11 | 0.11 | [18] |
| $T_m$ (°C) | 172 | 172 | 172 | [62] |
| $T_g$ (°C) | -10 | -10 | -10 | [62] |
| $C \times 10^{-10}$ ($cm^2$/dyn) | 9.0 | 9.0 | 9.0 | [62] |
| $\Delta n_c^o$ | 0.029 | 0.029 | 0.029 | [63] |
| $\Delta n_a^o$ | 0.06 | 0.06 | 0.06 | [63] |
| *Constitutive equation* | | | | |
| $s$ | 0.00324 | 0.000974 | 0.00118 | [48] |
| $T_b$ (K) | 4794 | 4374 | 4548 | [48] |
| $A_1$ (Pa s) | $2.120 \times 10^{-2}$ | $8.640 \times 10^{-2}$ | $6.180 \times 10^{-2}$ | [48] |
| $A_2$ (Pa s) | $1.820 \times 10^{-1}$ | 1.120 | 1.980 | [48] |
| $A_3$ (Pa s) | $1.480 \times 10^{-1}$ | 1.800 | 2.180 | [48] |
| $B_1$ (s) | $2.800 \times 10^{-7}$ | $8.480 \times 10^{-7}$ | $5.640 \times 10^{-7}$ | [48] |
| $B_2$ (s) | $1.180 \times 10^{-5}$ | $2.340 \times 10^{-5}$ | $4.480 \times 10^{-5}$ | [48] |
| $B_3$ (s) | $3.420 \times 10^{-4}$ | $5.840 \times 10^{-4}$ | $7.280 \times 10^{-4}$ | [48] |
| *Thermal properties* | | | | |
| $k$ (W/m K) | 0.193 | 0.193 | 0.193 | [62] |
| $C_p$ (J/kg K) | 2140 | 2140 | 2140 | [62] |
| $\rho$ ($kg/m^3$) | 900 | 900 | 900 | [62] |

material constants such as the parameter, $s$, the number of relaxation mode, $N$, and the viscosity, $\eta_k$, and relaxation time, $\theta_k$, were determined from these rheological experiments. The material constants, including $A_k$, $B_k$, $T_b$, $N$ and $s$, were obtained by curve fitting of the viscosity data as a function of shear rates at three temperatures of 180, 200, and 230 °C using Eqs. (10)–(12) and (32). The least square nonlinear regression method was used for curve fitting, and fitted parameters are listed in Table 2. As an example, the measured data along with fitted curves for PP-6523 are illustrated in Fig. 3 [48].

The pressure trace within the mold was measured, and the crystallization factor $f_{cr}$ was adjusted in such a way that the best fit to the pressure trace is obtained. In the case of i-PPs, the obtained crystallization factor $f_{cr}$ had a value of 0.11 [18], which shows that the interfacial energy changes caused by the high nucleation density are in the same order of the volume energy changes caused by crystallization. The same crystallization factor was used to predict the flow-induced crystallization of a wide variety of operation points for the three isotactic polypropylenes of different molecular weights.

Parameters for the Spencer–Gilmore *PVT* equation, Eqs. (34)–(37), are taken from Ref. [25] and listed in Table 4.

## 4. Meshes and numerical scheme

The numerical simulations of the injection molding process of i-PPs were carried out. The simulation code was developed using ANSI C programming language. The mesh network was generated over the mold cavity and the melt delivery system, which was divided into 12 segments based upon the geometric continuity. Each of these segments does

Table 3
Processing conditions for the injection molding experiment for i-PPs [46]

| Condition number | Holding time (s) | Injection speed ($cm^3$/s) | Melt temperature (°C) | Mold temperature (°C) |
|---|---|---|---|---|
| 1 | 15 | 49.00 | 215 | 25 |
| 2 | 15 | 49.00 | 230 | 25 |
| 3 | 15 | 12.25 | 230 | 25 |
| 4 | 15 | 122.5 | 230 | 25 |
| 5 | 5 | 49.00 | 230 | 25 |
| 6 | 30 | 49.00 | 230 | 25 |
| 7 | 15 | 49.00 | 230 | 60 |
| 8 | 15 | 49.00 | 250 | 25 |

Cooling time: 20 s. Packing pressure: 44.8 MPa.

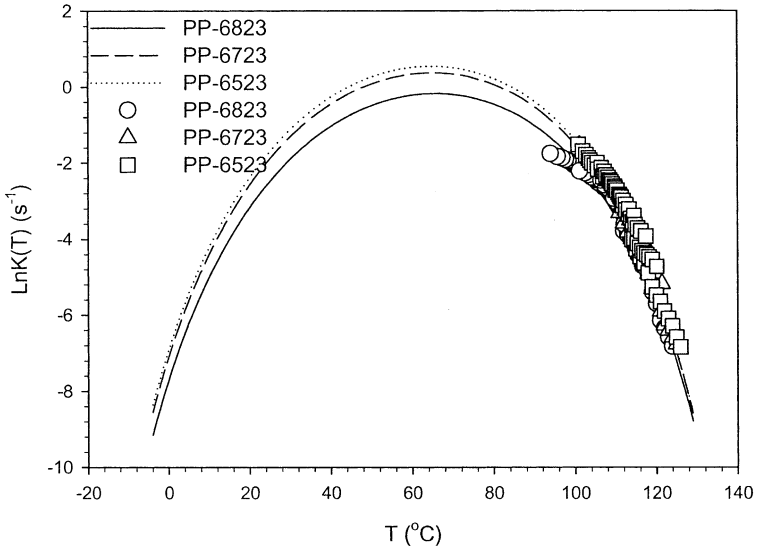


Fig. 2. Non-isothermal crystallization rate constants for various i-PPs [15]. Experimental data (symbols) with non-linear regression (lines) fit to non-isothermal rate constant in Eq. (56) at the quiescent condition.

not contain any juncture with the cross section of the flow channel having the same geometric shape (circular or rectangular). These 12 segments were discretized into equally spaced 182 nodes in the flow direction. The half thickness in the melt delivery system and the cavity was discretized into 65 equally-spaced nodes.

At the sprue entrance the gapwise distribution of temperature is assumed to be uniform and equal to the inlet melt temperature, $T_o$. Presumably, the melt front, $x_f$, progresses regularly, starting from the gate to the end of cavity. That means the melt front, $x=x_f$, advances one space of $\Delta x$ at the time step of $\Delta t$. The melt front flow can be thought of as the steady, fully developed Poiseuille-type. In this case, the system of equations for the elastic strain tensor, composed of Eqs. (20)–(22), is reduced from the system of differential equations to that of algebraic equations. The analytical solutions for the shear rate dependent elastic strain tensor components of $k$th mode at the melt front, $C_{ij,k}(x_f,y_j,t)$ (which are the initial values at the node of $(x_f,y_j)$ for the subsequent time steps, $t+\Delta t$) are given by Eqs. (29)–(31). At the same time, the shear rates, $\dot{\gamma}(x_f,\ y_j,\ t)$, and the elastic tensor components of $k$th mode, $C_{ij,k}(x_f,y_j,t)$, should satisfy Eqs. (19) and (27) (Cartesian), or (28) (cylindrical), as dictated by the viscoelastic constitutive equation and transport laws. Therefore, Eqs. (19), (27) (Cartesian), (28)) (cylindrical), and Eqs. (29)–(31) can be considered as the system of equations for the shear rate, $\dot{\gamma}(x_f,\ y_j,\ t)$, which can be solved by Newton–Raphson

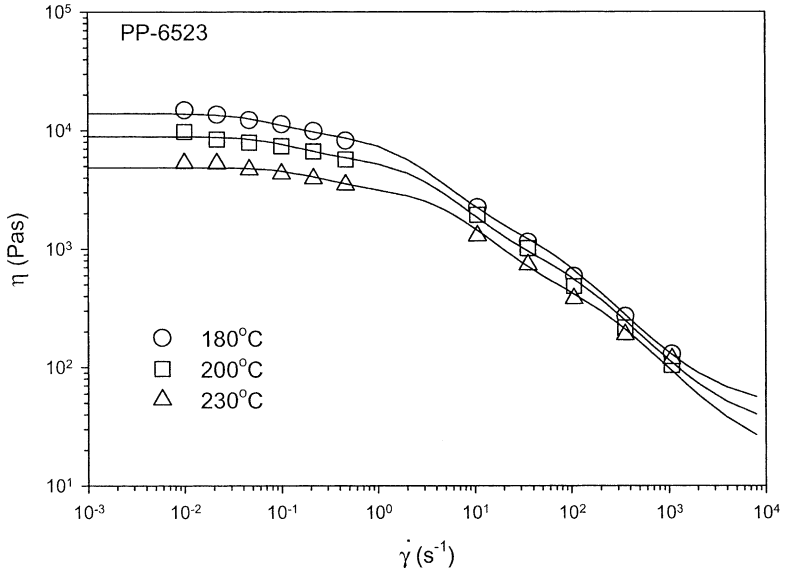


Fig. 3. Flow curves at various melt temperatures as a function of shear rate for PP-6523. Symbols represent the experimental data [64] while lines indicate the non-linear regression fit to Eqs. (10)–(12) and (32).

Table 4
Material constants in Spencer–Gilmore *P–V–T* equation of state

| Unit | $T \geq T_t$ | $T \leq T_t$ |
|---|---|---|
| $\bar{P}$ ($10^8$ Pa) | 2.650 | 2.402 |
| $\bar{R}$ ($10^2$ J/kg K) | 2.203 | 1.029 |
| $\bar{\rho}$ ($10^3$ kg/m$^3$) | 1.084 | 1.005 |
| $b_5$ ($10^2$ K) | 3.960 | |
| $b_6$ ($10^{-7}$ K/Pa) | 2.250 | |
| $b_7$ ($10^{-5}$ m$^3$/kg) | 8.700 | |
| $b_8$ ($10^{-1}$ K$^{-1}$) | 5.370 | |
| $b_9$ ($10^{-7}$ kg/m$^3$) | 1.260 | |

iterative method [49]. The initial guess for the shear rate, $\dot{\gamma}(x_f,\ y_j,\ t)$, are given by [4]:

$$\dot{\gamma}^0(x_f, y_j, t) = \frac{3U}{b^2} y_j \quad \text{(Cartesian coordinates)} \tag{73}$$

$$\dot{\gamma}^0(x_f, y_j, t) = \frac{4U}{b^2} y_j \quad \text{(cylindrical coordinates)} \tag{74}$$

Starting from the initial guess so determined, the iterative solution procedure based on Newton–Raphson method is carried out until the solutions for the elastic strain tensors and shear rates at the melt front are converged.

In computation, the melt front was advanced along the flow direction until the end of the cavity is reached. For the nodes other than those at the melt front and the gate in the flow domain, $(x_i,y_j)$ with $i \neq f$, the iterative method with the numerical relaxation must be utilized to directly solve the system of equations composed of Eqs. (19) and (27) (Cartesian), or Eq. (28) (cylindrical), and Eqs. (20)–(22) with $C_{ij,k}(x_i,y_j,t)$ and $\dot{\gamma}(x_i,\ y_j,\ t)$ at the node $(x_i,y_j)$ as the unknowns. The initial guess for each of the unknowns is its value at the previous time, namely, $C_{ij,k}(x_i,y_j,t-\Delta t)$ and $\dot{\gamma}(x_i,\ y_j,\ t-\Delta t)$. The shear rates and the elastic strain tensor components are numerically determined using the convergence parameters.

The convective term in Eqs. (20) and (21) was handled using newly calculated time step, $\Delta t'$, by considering flow in filling and packing stage:

$$\Delta t' = \frac{1}{1/\Delta t + u(x_i, y_j, t)/\Delta x} \tag{75}$$

Using the converged value of $C_{ij,k}(x_i,y_j,t)$, stress tensor $\tau_{ij}(x_i,y_j,t)$, reduction of entropy $\Delta S_{el}(x_i,y_j,t)$, velocity $v(x_i,y_j,t)$, and relative crystallinity $\theta(x_i,y_j,t)$ are updated. If the mold cavity is filled, then filling stage is complete and packing stage starts.

During the packing stage, high pressure is applied at the sprue entrance. Consequently, the density $\bar{\rho}$ within the mold geometry does vary with time. Thus, the *PVT* equation of state proposed by Spencer and Gilmore is employed to take into account the compressibility of the polymer melt. With taking the representative density, $\bar{\rho} = \bar{\rho}(x,t)$, the general form of the unified governing equation of flow can be attained for the packing stage by substituting Eqs. (39)–(41) into Eq. (49) [2]:

$$G(x,t)\frac{\partial P}{\partial t} - \frac{\partial}{\partial x}\left(S\frac{\partial P}{\partial x}\right) = F(x,t) \tag{76}$$

where

$$G(x,t) = \frac{1}{\bar{\rho}(P+\hat{P})}\int_0^b \rho\left(1-\rho\hat{\rho}\right)\mathrm{d}y \tag{77}$$

$$F(x,t) = 1\bar{\rho}\int_0^b \rho\left(1-\rho\hat{\rho}\right)\frac{\partial \ln T}{\partial t}\mathrm{d}y \tag{78}$$

It is noted that the representative density $\bar{\rho} = \bar{\rho}(x,t)$, should be evaluated using Eq. (50) to avoid its dependence on the gapwise direction. Eq. (76) would be used to update the pressure profile during the packing stage. This is possible since the packing stage immediately follows the filling stage, at the end of which the information on $P$, $T$, $\rho$ and $S$ are known. Based upon the quantities at the previous time, the pressure at the current time could be determined by solving Eq. (76). The procedure continues until the packing stage ends. Once the pressure profile $P(x,t)$ is updated, the pressure gradient $\Lambda(x,t)$ can be calculated based upon the known pressure profile, and the fluidity $S(x,t)$ updated at the same time. Furthermore, shear rate $\dot{\gamma}(x,y,t)$, velocity $u(x,y,t)$ and energy dissipation $\Phi(x,y,t)$ can be computed for each instant of time in the same way as that for the filling stage except using additional pack flow rate, $Q_{\text{pack}}$, instead of flow rate in filling stage. $Q_{\text{pack}}$ is calculated by the difference of specific volume combined with the cavity volume using Eqs. (34)–(38):

$$Q_{\text{pack}} = \left|\frac{V(T(t),P(t),X_c(t)) - V(T(t-\Delta t),P(t-\Delta t),X_c(t-\Delta t))}{\Delta t}\right| \tag{79}$$

In addition, the densities, $\rho(x,y,t)$ and $\bar{\rho}(x,t)$ are also updated accordingly.

In the cooling stage, the flow is ceased. Therefore, the velocity and shear rates are zero. The flow stresses developed during the filling and packing stage relax, governed by the viscoelastic constitutive equation, Eqs. (20)–(22). Therefore, the numerical computation scheme for the relaxation of the flow stresses is greatly simplified in comparison with that of filling and packing stage. The computational procedure is similar to that explained in filling stage, except that the calculations related to the flow field disappear with $\dot{\gamma} = u \equiv 0$.

## 5. Results and discussion

### 5.1. Elastic recovery and crystallization orientation function

Molecular chains in an extended state relax at the removal of the stress. However, the elastic strain may not

relax completely depending on the material characteristics, temperature, crystallinity and so on. The elastic strain can be frozen-in when the polymer material passes through the crystallization temperature, or when the degree of crystallinity exceeds a certain level. The unrelaxed portion of the elastic strain is considered as 'elastic recovery', which can be used for the evaluation of birefringence.

Fig. 4 illustrates the calculated total strain, transient elastic recovery (elastic strain) and plastic strain as a function of time for PP6523 at the processing temperature of 215 °C and the shear rate of 500 $s^{-1}$. Clearly, the total strain increases linearly with time and its value is close to that of the elastic recovery at the start of the shear flow at low times. On the other hand, the plastic strain which is much lower than the total strain and elastic recovery at the start of the shear flow, increases with time and then reaches the total strain at large times upon achieving the steady state flow. The elastic recovery passes through an overshoot before reaching its steady state value.

Fig. 5 illustrates the transient elastic recovery as a function of time after start-up of steady shear flow under an isothermal condition at various shear rates for PP-6523 calculated according to Eqs. (65)–(69). The elastic recovery increases linearly with time at small times, and then deviates from linear behavior, overshoots, finally reaches a steady state value. The overshoot position shifts to lower time with increasing shear rate, and the elastic recovery increases with shear rate. The elastic recovery may achieve a value as high as 10. Certainly, it is the main source for introducing the orientation and development of birefringence.

Fig. 6 shows the dependence of the ultimate elastic recovery on shear stress in steady-state shear flow obtained for various processing temperatures of $T_p$ = 185–270 °C for PP-6523 and -6723 calculated according to Eqs. (66)–(69). It is seen that for each i-PP a master curve of the ultimate elastic recovery is obtained, which is independent of processing temperatures. At the same shear stress, the elastic recovery is larger in low molecular weight PP-6523 than in higher molecular weight PP-6723 till a certain value of the shear stress. However, the maximum attainable elastic recovery is larger in case of PP-6723.

Fig. 7 shows the transient crystalline orientation function at various shear rates for PP-6523 calculated according to Eqs. (71)–(72). The crystalline orientation function becomes higher at high shear rates, and reaches the steady-state value faster with the increase of shear rate.

The ultimate crystalline orientation function versus shear stress in steady state flow at various processing temperatures ($T_p$ = 185–270 °C) for PP-6723 and -6523 is illustrated in Fig. 8. The crystalline orientation function is independent of the processing temperature. It is linearly proportional to the shear stress at its low values and deviates from linearity with an increase in shear stress. It reaches a value close to 1 at higher shear stress.

Figs. 9 and 10 show, respectively, the ultimate elastic recovery and the crystalline orientation function at steady state flow as a function of the processing temperature at various shear rates for PP-6523 calculated according to Eqs. (66)–(72). The ultimate elastic recovery and crystalline orientation function increase with increasing shear rate and decreasing processing temperature.

Fig. 11 shows the transient elastic recovery as a function of time at the shear rate of 500 $s^{-1}$ and the processing temperature of 195 °C for i-PPs having different molecular weights calculated according to Eqs. (65)–(69). At low time, the elastic recovery is independent of the molecular weight. However, at larger time before reaching steady state the overshoot appears with its position on time scale shifted towards larger time. This overshoot increases with the

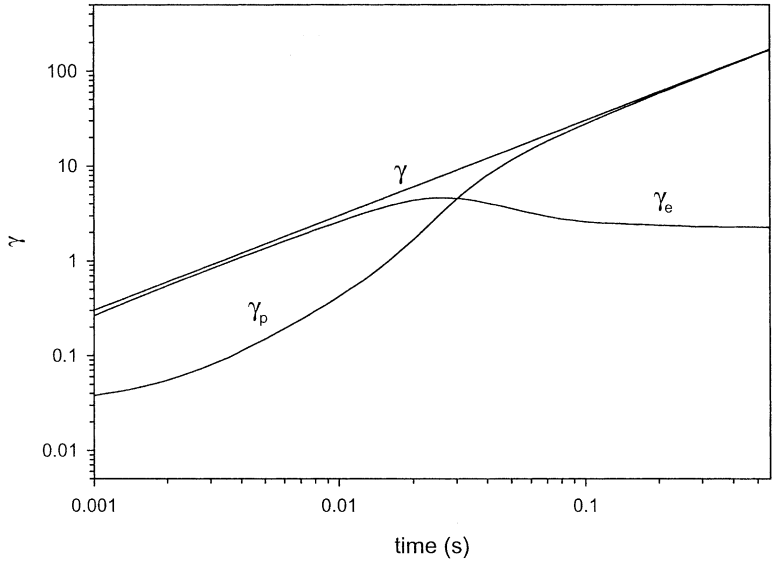


Fig. 4. Calculated total strain, transient elastic recovery and plastic strain as a function of time for PP6523 at $T_p$ = 215 °C, $\dot{\gamma}$ = 500 $s^{-1}$.

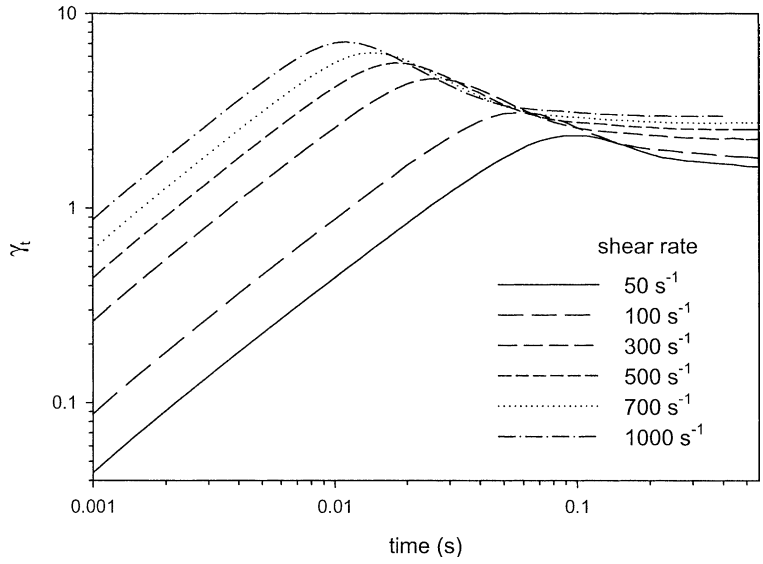


Fig. 5. Transient elastic recovery as a function of time after the start-up of steady shear flow at various shear rates for PP-6523 at $T_p = 215$ °C calculated according to Eqs. (65)–(69).

molecular weight. Also, the steady-state value of elastic recovery increases with the molecular weight.

### 5.2. Pressure and birefringence distribution

Fig. 12 shows pressure traces during the injection molding for filling stage and beginning of packing stage (a) and complete molding cycle (b) for PP-6523. Both experimental and predicted pressure traces are shown in these figures with the symbols representing the recorded pressure at three transducer locations and lines representing the corresponding predicted pressure traces. Generally, the simulated pressure traces during the filling stage and at the beginning of the packing stage are in a good agreement with the experimental data. It can be seen that the experimental pressure traces rise quickly to the maximum at the end of the filling stage, overshoot at the beginning of the packing stage and then reach constant values corresponding to the holding pressure and maintain their values during holding time. This pressure overshoot is due to a sudden imposition of holding pressure. Namely, it takes some time for the pressure to achieve the steady packing pressure that applied to the melt at the beginning of the packing stage. However, in the simulation, the holding pressure is taken as the input parameter and therefore this overshoot is not seen. Accordingly, the pressure trace obtained from the simulation can not very well describe the pressure traces observed in the experiment at the beginning of the packing

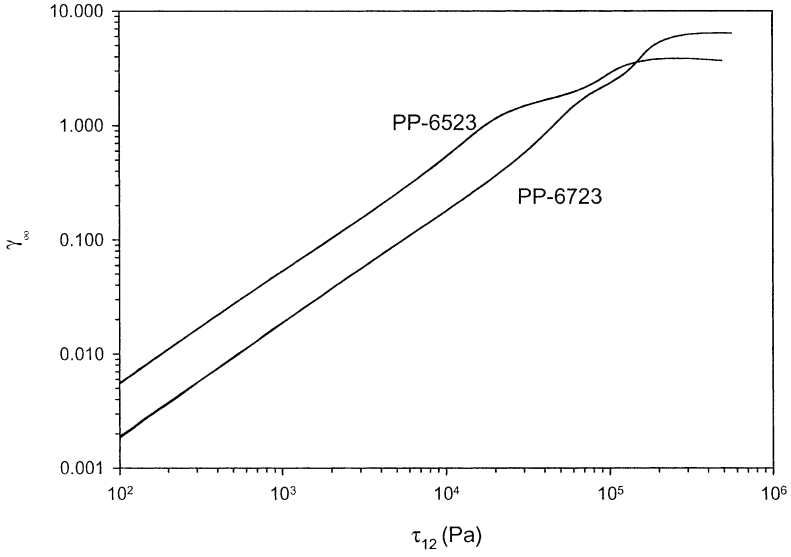


Fig. 6. Dependence of the elastic recovery on shear stress during shear flow at various processing temperatures of $T_p = 185$–$270$ °C for PP-6523 and -6723 calculated according to Eqs. (66)–(69).

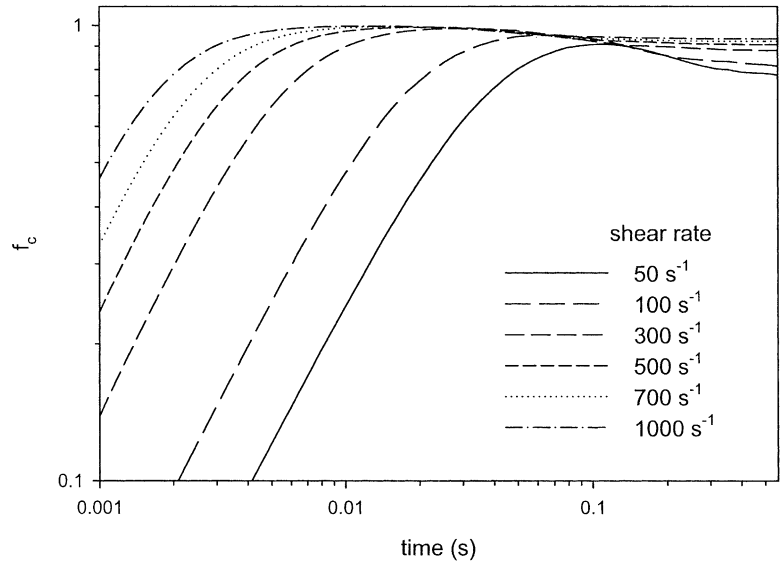


Fig. 7. Crystalline orientation function as a function of time after start-up of shear flow at various shear rates for PP-6523 at $T_p = 195$ °C calculated according to Eqs. (71) and (72).

stage. Nevertheless, the flow-induced crystallization occurs in the filling stage, so this should not have an appreciable effect in simulation of the flow-induced crystallization.

In the cooling stage, the experimental pressures relax very fast in comparison with the predicted pressure. In molding experiments, the screw retracts immediately after removing the holding pressure leading to the fast decay of pressure in the cavity. This effect was not included in the present simulation.

### *5.2.1. Birefringence distribution*

The birefringence in the injection molding of semicrystalline polymers appears as a result of two contributions, namely crystalline and amorphous.

According to [2], the birefringence in moldings made of amorphous polymers appears from two main sources. The first is the flow-induced birefringence, which is a consequence of the shear and normal stresses developing during cavity filling and packing leading to the orientation of molecular chains. During the subsequent cooling stage this orientation does not completely relax and appears as the frozen-in birefringence in moldings. The second source of the birefringence in moldings of amorphous polymers is the non-equilibrium density or shrinkage change and the viscoelastic behavior of the polymer during the inhomogeneous rapid cooling through $T_g$, which results in the thermal birefringence. In the past decades, the theoretical description of birefringence in molded parts of amorphous

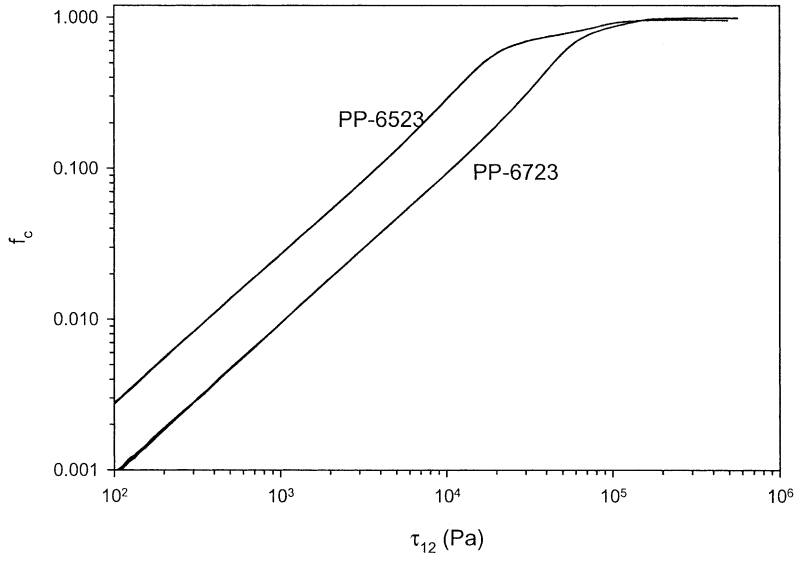


Fig. 8. Dependence of the crystalline orientation function on shear stress during shear flow at various processing temperatures at $T_p = 185$–270 °C for PP-6523 and -6723 calculated according to Eqs. (71) and (72).

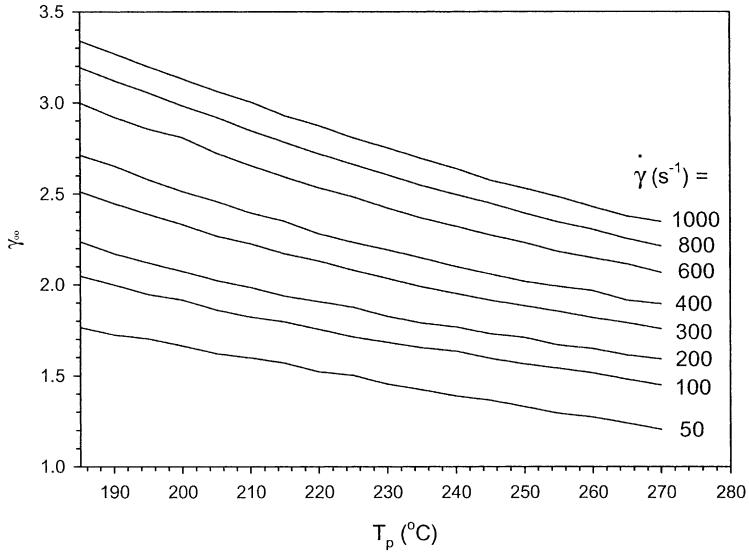


Fig. 9. Processing temperature effect on the ultimate elastic recovery at various shear rates for PP-6523 calculated according to Eqs. (66)–(69).

polymers has been widely studied by many authors [2–6,11, 50]. However, for semicrystalline polymers, there are only a few theoretical studies on the frozen-in birefringence. It is due to the complexity of its prediction [51–54]. In particular, the overall birefringence of the semicrystalline polymers is attributed by both crystalline and amorphous contributions.

In this study, it is assumed that the stress and elastic recovery freeze at the onset of flow-induced crystallization during the filling stage. In the packing and cooling stage the isotropic melting temperature was used for this purpose. This is reasonable because the flow rate during packing stage is not large, although the temperature becomes low. The frozen-in elastic recovery can be calculated more appropriately by using the crystallinity-dependent viscosity without the necessity of making any assumption about freezing condition. However, experiments to relate the crystallinity to viscosity are very difficult to carry out especially at high shear rates occurring during injection molding, although some limited experimental data at low shear rates were reported concerning the viscosity increase due to the crystallization [29,55,56]. Clearly, more studies are required to elucidate the issues related to the crystallinity-dependent viscosity.

In the present study, the frozen-in elastic recovery was used to calculate the principal extension ratio, $\lambda$ and the crystalline orientation function, $f_c$, to determine the crystalline contribution to the overall birefringence. At same time, the flow birefringence, calculated by using the stress-optical

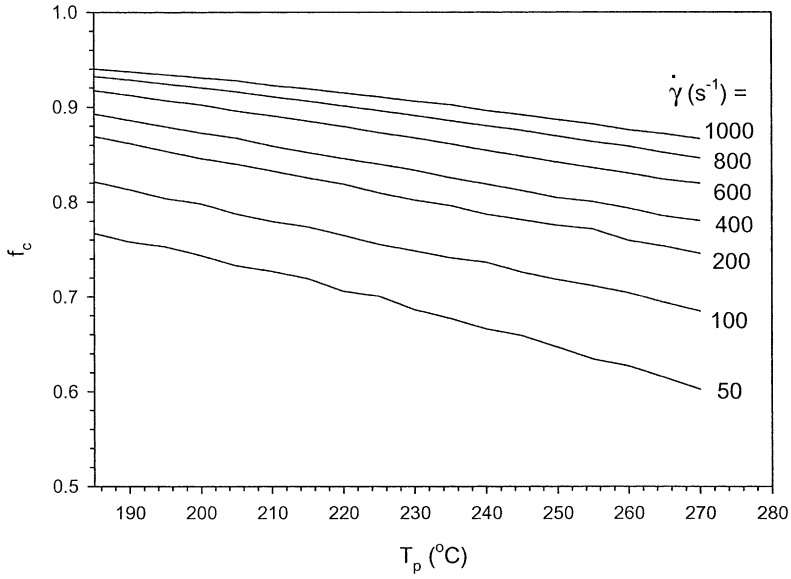


Fig. 10. Processing temperature effect on the crystalline orientation function at various shear rates for PP-6523 calculated according to Eqs. (66)–(72).

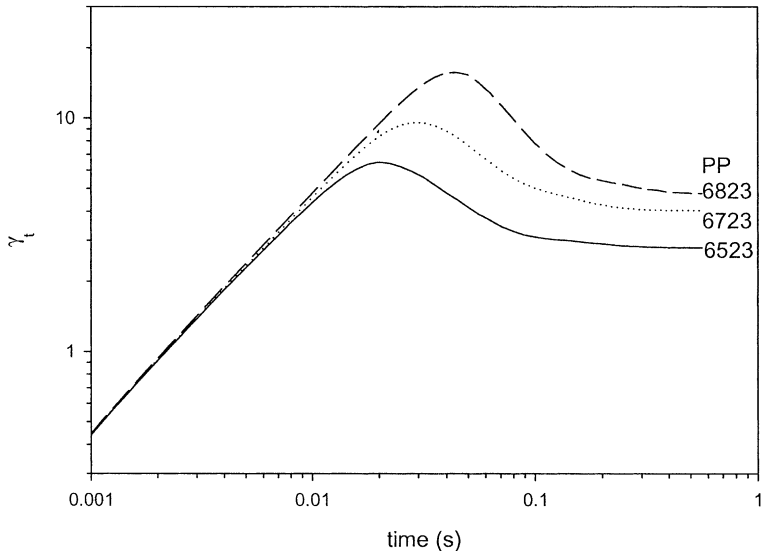


Fig. 11. Transient elastic recovery as a function of time for PP-6523, -6723 and -6823 at $T_p = 195$ °C and $\dot{\gamma} = 500\ s^{-1}$ calculated according to Eqs. (65)–(69).

rule, was used to determine the amorphous contribution to the overall birefringence.

Figs. 13–18 show the gapwise distribution of the frozen-in birefringence at the midway of moldings for various i-PPs at different processing conditions. From these figures, one can see that the positions near the wall show significantly higher birefringence than the positions near the center of the moldings. This indicates the higher orientation of the molecules at the positions near the wall. The high shear rate near the wall causes the flow-induced crystallization in this region leading to the formation of a skin layer. The skin layer is generally thought to exhibit the shish-kebab structure, which has the higher orientation [13,14–18,54,57,58].

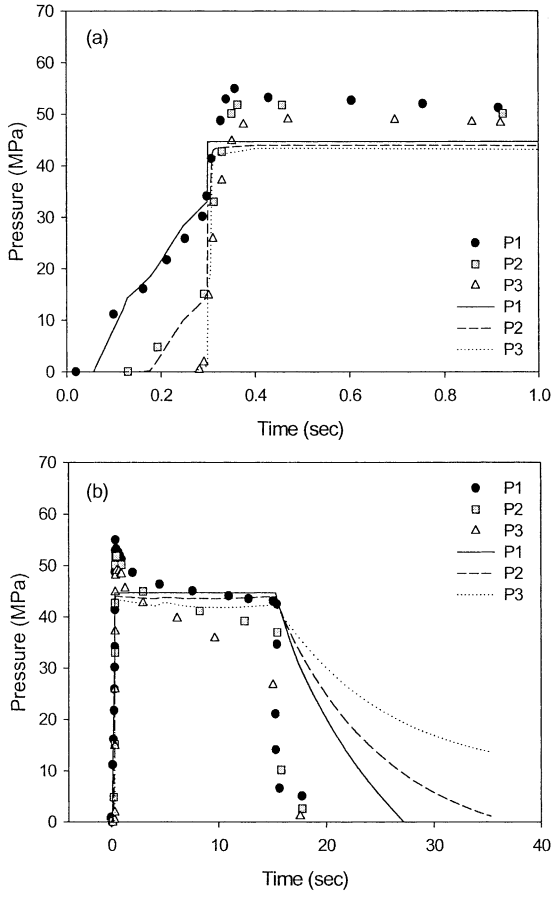


Fig. 12. Experimental [46] (symbols) and simulated (lines) cavity pressure traces of dumbbell shape cavity at locations P1, P2 and P3 for PP-6523, $T_0 = 230$ °C, $T_w = 25$ °C, $t_h = 15$ s, $P_h = 44.8$ MPa and $Q = 49.0\ cm^3/s$ at condition 2 in Table 3.

Typically, a sharp decrease in birefringence from the skin to core is shown in these figures. The higher shear rate near the wall causes molecular chains to stretch and orient more in the flow direction, while in the core region this strong orientation does not occur due to low shear rates and high temperatures. This leads to the higher birefringence in the skin than that in the core. Therefore, the birefringence measurement can be used to estimate the effect of the flow-induced crystallization [13,14–18,52,59,60].

In the core region of the moldings, the quiescent crystallization occurs under the non-isothermal conditions. The crystallization front moves away from the mold walls towards the core due to the temperature gradient in the thickness direction. This causes the creation of spherulites with the slight preferential orientation as indicated by the non-zero value of birefringence in the core. The study of birefringence distribution in moldings of amorphous polymers [2,4–12] also showed the non-zero residual birefringence in the core. It was mentioned that the non-zero residual birefringence in the core is derived from the residual thermal birefringence. Thus, it can be thought that the birefringence in the core of semicrystalline polymer is also affected by thermal stresses developed in both crystalline and amorphous regions.

Fig. 13 depicts the effect of melt temperature for

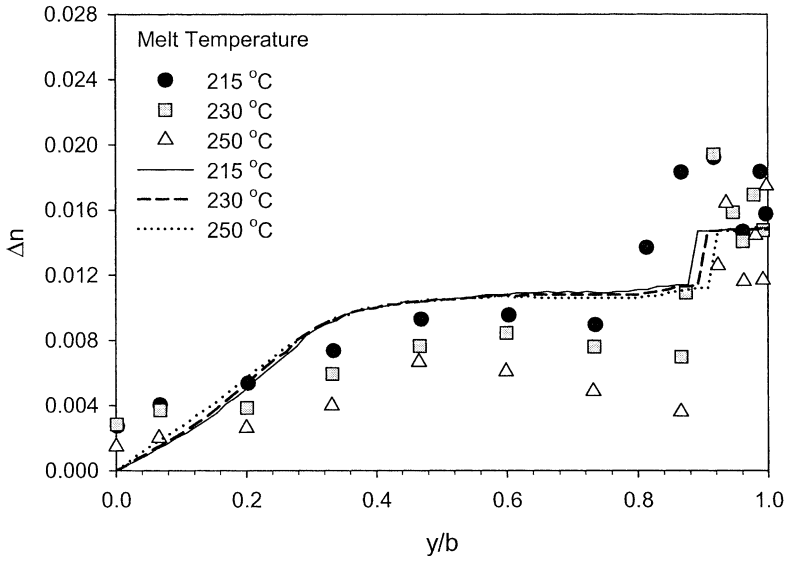


Fig. 13. Gapwise birefringence distribution at the midway of dumbbell shape cavity moldings of PP6523 at different inlet melt temperatures. Symbols represent the experimental data while lines indicate the simulated data. Molding conditions are 1, 2 and 8 in Table 3: $Q=49$ cm$^3$/s, $P_h=44.8$ MPa, $t_h=15$ s and $T_w=25$ °C.

PP-6523. A decrease in the inlet melt temperature causes a slight increase of the value of birefringence in the scin layer near the wall. However, thicker skin layers are observed with a decrease of the inlet melt temperature. This is due to an increase in the relaxation time of the flow-induced crystallization with decreasing the inlet melt temperature [53,60], which leads to the highly oriented skin layer. At the core, comparatively high level of birefringence is observed due to an additional flow occurring during the packing stage. Simulated data also predict the development of birefringence in this region. As is evident from Fig. 15, the birefringence in the core region mainly arises due to the presence of packing stage as indicated by calculated results. The prediction of birefringence without packing stage shows no birefringence at this region. However, in contrast to experiments simulated data does not show the strong effect of melt temperature on birefringence in the core region.

From Fig. 14, one can see the effect of holding times on the birefringence of PP-6523. According to the experimental data, holding time does not affect the skin layer thickness and birefringence. However, when the holding time increases, the birefringence in the core region also increases. As cooling continues after cavity is filled, the material in the

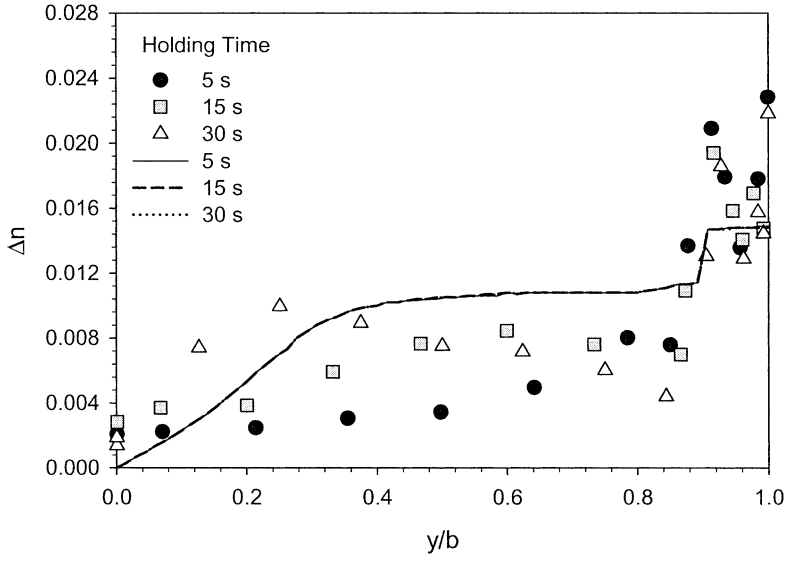


Fig. 14. Gapwise birefringence distribution at the midway of dumbbell shape cavity moldings of PP6523 at different holding times. Symbols represent the experimental data while lines indicate the simulated data. Molding conditions are 2, 5 and 6 in Table 3: $Q=49$ cm$^3$/s, $P_h=44.8$ MPa, $T_m=230$ °C and $T_w=25$ °C.

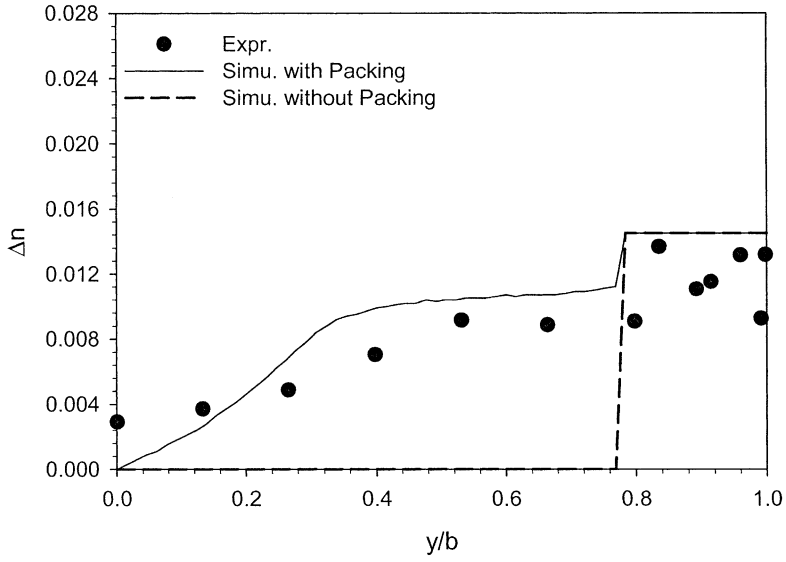


Fig. 15. Comparison of the prediction of the gapwise birefringence distribution with and without packing stage at the midway of dumbbell shape cavity moldings of PP6523. Symbols represent the experimental data while lines indicate the simulated data. Molding condition is 3 in Table 3: $P_h$=44.8 MPa, $T_m$=230 °C, $t_h$=15 s and $T_w$=25 °C.

cavity undergoes contraction, thus creating a space for the additional material to flow into the cavity. During the holding time, the packing pressure is imposed, thus the additional material will get supplied to the cavity. Accordingly, the deformation process in the material continues during this stage. Such deformation proceeds under high stress, thereby introducing high orientation [2]. However, in contrast to experiments simulated data does not show the effect of holding time on the birefringence in the core region. This is due to the fact that the isotropic melting temperature was used as an assumption to determine freezing in the packing stage. In addition, thermally induced birefringence during crystallization is not considered in this study. If the crystallinity-dependent viscosity and thermally induced birefringence are considered, the freezing of molecular chains would occur naturally. Then the effect of holding time or holding pressure on the birefringence in the core region would be predicted more correctly.

The effect of wall temperature on the birefringence is shown in Fig. 16 for PP-6723. The skin layer thickness and birefringence at the core region decreases as the wall temperature increases. As a result of increasing wall temperature, the cooling rate decreases, which leads to a less oriented material due to the possibility for a more relaxation [60,61]. The simulated data are seen to show a fair agreement with experiments.

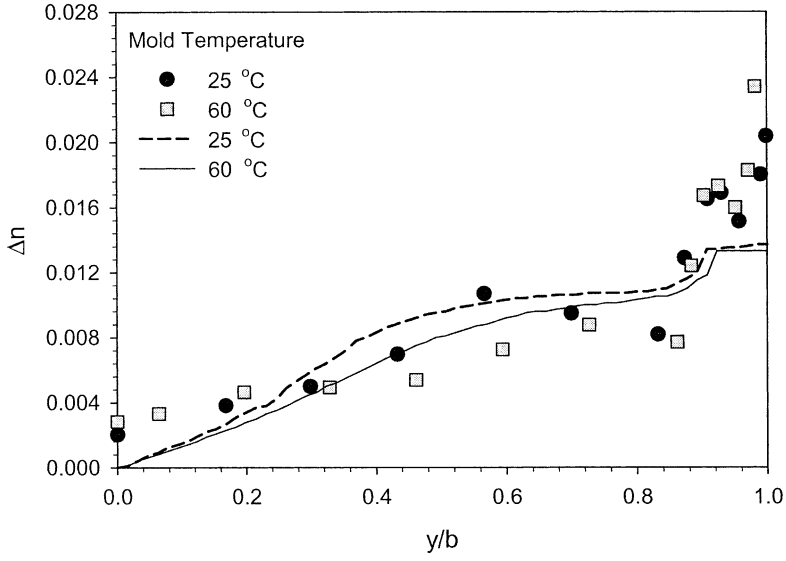


Fig. 16. Gapwise birefringence distribution at the midway of dumbbell shape cavity moldings of PP6723 at different mold temperatures. Symbols represent the experimental data while lines indicate the simulated data. Molding conditions are 2 and 7 in Table 3: $Q$=49 cm$^3$/s, $P_h$=44.8 MPa, $T_m$=230 °C and $t_h$=15 s.

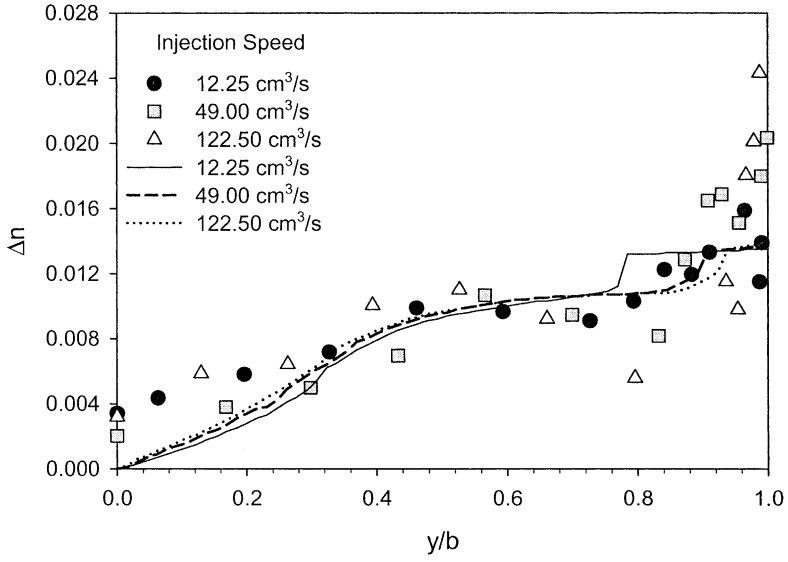


Fig. 17. Gapwise birefringence distribution at the midway of dumbbell shape cavity moldings of PP6723 at different injection speeds. Symbols represent the experimental data while lines indicate the simulated data. Molding conditions are 2, 3 and 4 in Table 3: $P_h$=44.8 MPa, $T_m$=230 °C, $t_h$=15 s and $T_w$=25 °C.

Fig. 17 illustrates the effect of injection speed on the birefringence for PP-6723. The skin layer thickness increases with decreasing the injection speed. Both the simulated and experimental data show this tendency. However, simulated results are unable to predict the birefringence in the core region near the center line because in the present calculations only the contribution of the flow birefringence is considered without considering contribution of the thermal birefringence.

Fig. 18 shows the effect of molecular weight on the frozen-in birefringence. Clearly, the birefringence increases with the molecular weight. It is known that the relaxation time of polymer melts increases with an increase of molecular weight. The high relaxation time contributes to the high molecular orientation. Both the simulated and experimental birefringence of i-PPs shows this tendency.

## 6. Conclusion

In the processing of semicrystalline polymer, the flow-induced crystallization inherently occurs under non-isothermal flow conditions. Thus, the flow-induced crystallization plays a major role in determining the resultant microstructure and birefringence, and end-use

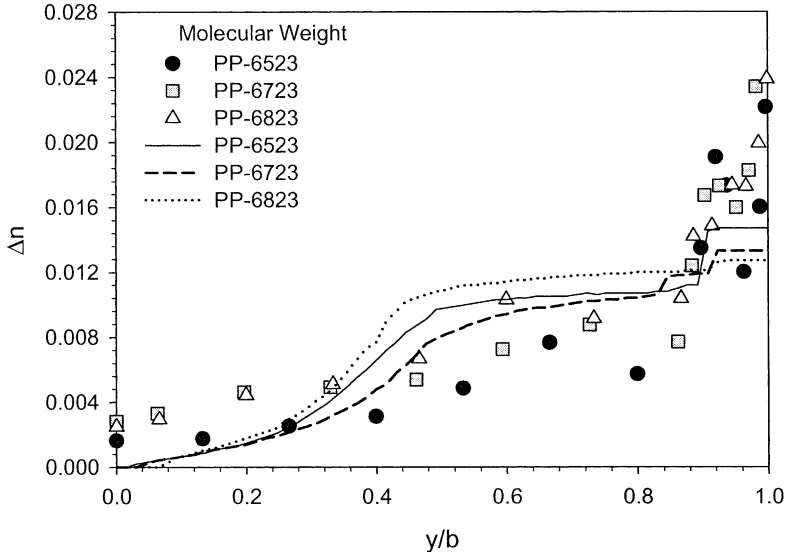


Fig. 18. Gapwise birefringence distribution at the midway of dumbbell shape cavity moldings of PP-6723, PP-6723 and PP-6823. Symbols represent the experimental data while lines indicate the simulated data. Molding condition is 7 in Table 3: $P_h$=44.8 MPa, $T_m$=230 °C, $Q$=49 cm$^3$/s, $t_h$=15 s and $T_w$=60 °C.

physical and optical properties. Simulation of the flow-induced crystallization and birefringence development was carried out based on the melting temperature elevation due to entropy reduction caused by flow of a non-linear viscoelastic fluid. Total frozen-in birefringence in moldings was calculated based on crystalline contribution determined upon freezing of crystalline orientation function at the elevated melting temperature during cavity filling and equilibrium melting temperature during packing and amorphous birefringence developed during molding cycle. In agreement with experiments, the calculation indicates that the melt temperature, injection speed, molecular weight and wall temperature affect the flow-induced crystallization and the amount of frozen-in birefringence in moldings. However, the present calculations show that these processing conditions and also holding pressure and holding time have less effect on the calculated frozen-in birefringence than the experiments indicated.

## Acknowledgements

This work is supported in part by the grant DMI-0322920 from the National Science Foundation, Division of Engineering.

## References

[1] De Vries AJ, Bonnebat C, Beautemps J. Uni- and biaxial orientation of polymer films and sheets. J Polym Sci, Polym Symp 1977;58: 109–56.
[2] Isayev AI, editor. Injection and compression molding fundamentals. New York: Marcel Dekker; 1987.
[3] Isayev AI, Crouthamel DL. Residual stress development in the injection molding of polymers. Polym-Plast Tech Eng 1984;22(2): 177–232.
[4] Isayev AI, Hieber CA. Toward a viscoelastic modeling of the injection molding of polymers. Rheol Acta 1980;19(2):168–82.
[5] Isayev AI. Orientation development in the injection molding of amorphous polymers. Polym Eng Sci 1983;23(5):271–84.
[6] Janeschitz-Kriegl H, editor. Polymer melt rheology and flow birefringence. Berlin: Springer; 1983.
[7] Wales JLS, Van Leeuwen J, Van der Vijgh R. Orientation in injection molded objects. Polym Eng Sci 1972;12(5):358–63.
[8] Dietz W, White JL. A simple model for calculating the pressure loss during the mold filling stage and the frozen-in orientation in the injection molding of amorphous plastics. Rheol Acta 1978;17(6): 676–92.
[9] Greener J, Pearson GH. Orientation residual stresses and birefringence in injection molding. J Rheol 1983;27(2):115–34.
[10] Flaman AAM. Buildup and relaxation of molecular orientation in injection molding. Part I. Formulation. Polym Eng Sci e 1993;33(4): 193–201.
[11] Isayev AI, editor. Modeling of polymer processing: recent developments. Munich: Hanser; 1991.
[12] Shyu GD, Isayev AI. Residual stresses and birefringence in injection molded disks. SPE ANTEC 1995;41:2911–7.
[13] Guo X, Isayev AI. Residual stresses and birefringence in injection molding of semicrystalline polymer part 1: theoretical formulation. Int Polym Process 1999;14(4):377–86.
[14] Guo X, Isayev AI, Guo L. Crystallinity and microstructure in injection moldings of isotactic polypropylenes. Part 1: a new approach to modeling and model parameters. Polym Eng Sci 1999;39(10): 2096–114.
[15] Isayev AI, Catignani BF. Crystallization and microstructure in quenched slabs of various molecular weight polypropylenes. Polym Eng Sci 1997;37(9):1526–39.
[16] Isayev AI, Churdpunt Y, Guo X. Comparative study of Ziegler–Natta and metallocene based polypropylenes in injection molding: simulation and experiment. Int Polym Process 2000;15(1):72–82.
[17] Kim KH, Isayev AI, Kwon K. Flow-induced crystallization and birefringence in injection molding of semicrystalline polymers. SPE ANTEC 2003;49:713–7.
[18] Palluch KP, Isayev AI. Rheological modeling of stress-induced crystallization. Proceedings of the International Congress on Rheology, 13th, Cambridge, United Kingdom. 2 August 20–25, 2000. p. 94–6.
[19] Gaylord RJ. Orientation of crystallites formed in stretched polymeric networks. Polym Lett Ed 1975;13:337–40.
[20] Leonov AI. Nonequilibrium thermodynamics and rheology of viscoelastic polymer media. Rheol Acta 1976;15:85–98.
[21] Spencer RS. Volume–temperature–time relationships for polystyrene. J Coll Sci 1949;4:229–40.
[22] Spencer RS, Gilmore GD. Equation of state for polystyrene. J Appl Phys 1949;20:502–6.
[23] Spencer RS, Gilmore GD. Equation of state for high polymers. J Appl Phys 1950;21:523–6.
[24] Sobhanie M, Isayev AI. Viscoelastic simulation of flow of rubber compounds. Rubber Chem Tech 1989;62(5):939–56.
[25] Guo X, Isayev AI, Demiray M. Crystallinity and microstructure in injection moldings of isotactic polypropylenes. Part 2. Simulation and experiment. Polym Eng Sci 1999;39(11):2132–49.
[26] Hoffman JD. Theoretical aspects of polymer crystallization with chain folds: bulk polymers. SPE Trans 1964;4(4):315–62.
[27] George HH. Spinline crystallization of poly(ethylene terephthalate). In: Ziabicki A, Kawai H, editors. High-speed fiber spinning, 1985. p. 271–94.
[28] Flory PJ. Thermodynamics of crystallization in high polymers. I. Crystallization induced by stretching. J Chem Phys 1947;15:397–408.
[29] Kobayashi K, Nagasawa T. Crystallization of sheared polymer melts. J Macromol Sci, Phys 1970;4(2):331–45.
[30] Gaylord RJ. A theory of the stress-induced crystallization of crosslinked polymeric networks. J Polym Sci, Polym Phys Ed 1976; 14(10):1827–37.
[31] Katayama K, Yoon MG. Polymer crystallization in melt spinning: mathematical simulation. In: Ziabicki A, Kawai H, editors. High-speed fiber spinning. New York: Wiley; 1985. p. 207–23.
[32] Hay IL, Jaffe M, Wissbrun KF. A phenomenological model for row nucleation in polymers. J Macromol Sci, Part B 1976;12:423–8.
[33] Alfonso GC, Grimaldi D, Turturro A. Nonisothermal crystallization kinetics. Conv Ital Sci Macromol 1977;3:144–5.
[34] Ziabicki A. The mechanisms of 'neck-like' deformation in high-speed melt spinning. 1. Rheological and dynamic factors. J Non-Newton Fluid Mech 1988;30(2-3):141–55.
[35] Ishizuka O, Koyama K. Crystallization of running filament in melt spinning of polypropylene. Polymer 1977;18(9):913–8.
[36] Oono R, Miasaka K, Ishikawa K. Crystallization kinetics of biaxially stretched natural rubber. J Polym Sci 1973;11:1477–88.
[37] Kraus G, Gruver JT. Kinetics of strain-induced crystallization of a trans-polypentenamer. J Polym Sci 1972;10:2009–24.
[38] Nakamura K, Katayama K, Amano T. Nonisothermal crystallization of polymers. II. Consideration of the isokinetic condition. J Appl Polym Sci 1973;17(4):1031–41.
[39] Nakamura K, Watanabe T, Katayama K, Amano T. Nonisothermal crystallization of polymers. I. Relation between crystallization temperature, crystallinity, and cooling conditions. J Appl Polym Sci 1972;16(5):1077–91.

[40] Hoffman JD, Davis GT, Lauritzen JI. In: Hannay NB, editor. Crystalline and noncrystalline solids. Treatise on solid state chemistry, vol. 3. New York: Plenum Press; 1976. p. 774.
[41] Dunning WJ. Kinetics of crystallization of rubber. Trans Faraday Soc 1954;50:1115–27.
[42] Guo J, Narh KA. Simplified model of stress-induced crystallization kinetics of polymers. Adv Polym Tech 2002;21(3):214–22.
[43] Fleibner M. Kunststoffe 1973;63:597.
[44] Upadhyay RK, Isayev AI, Shen SF. Transient shear flow behavior of polymeric fluids according to the Leonov model. Rheol Acta 1981; 20(5):443–57.
[45] Treloar LRG. The physics of rubber elasticity. 2nd ed. Oxford: Clarendon Press; 1958. p. 342.
[46] Van Sweden C. MS Thesis,The University of Akron; 2000.
[47] Chan TV, Shyu GD, Isayev AI. Master curve approach to polymer crystallization kinetics. Polym Eng Sci 1995;35(9):733–40.
[48] Guo X. PhD Thesis, The University of Akron; 1999.
[49] Evens GA. Practical numerical analysis. New York: Wiley; 1995.
[50] Isayev AI. Thermal stresses. Encycl Polym Sci Eng 1989;16:747–67.
[51] Isayev AI, Chan TW, Gmerek M, Shimojo K. Injection molding of semi-crystalline polymers: characterization and modeling. SPE ANTEC 1994;40:587–92.
[52] Isayev AI, Chan TW, Shimojo K, Gmerek M. Injection molding of semicrystalline polymers. I. Material characterization. J Appl Polym Sci 1995;55(5):807–19.
[53] Isayev AI, Chan TW, Gmerek M, Shimojo K. Injection molding of semicrystalline polymers. II. Modeling and experiments. J Appl Polym Sci 1995;55(5):821–38.
[54] Koppelmann J, Fleischmann E, Leitner G. Structure oriented skin layers in injection molded plates of polypropylene. Rheol Acta 1987; 26(6):548–59.
[55] Hieber CA. Modeling/simulating the injection molding of isotactic polypropylene. Polym Eng Sci 2002;42(7):1387–409.
[56] Poitou A, Ammar A. A molecular model for flow induced crystallization of polymers. Macromol Symp 2002;185:243–55.
[57] Kantz MR, Newman HD, Stigale FH. Skin–core morphology and structure–property relations in injection-molded polypropylene. J Appl Polym Sci 1972;16(5):1249–60.
[58] Fujiyama M. Structure and properties of injection moldings of beta-crystal nucleator-added polypropylene. Part 2. Effect of MFI of base resin. Int Polym Process 1995;10(3):251–4.
[59] Eder G, Janeschitz-Kriegl H, Liedauer S. Crystallization processes in quiescent and moving polymer melts under heat transfer conditions. Prog Polym Sci 1990;15(4):629–714.
[60] Guo L. MS Thesis, The University of Akron; 1995.
[61] Demiray M. MS Thesis, The University of Akron; 1996.
[62] Van Krevelen DW. Properties of polymers. Amsterdam: Elsevier; 1990.
[63] Brandrup J, Immergut EH. Polymer handbook. 3rd ed. New York: Wiley-Interscience; 1989. p. 453.
[64] Catignani B. MS Thesis, The University of Akron; 1996.